PROCEEDINGS A

rspa.royalsocietypublishing.org

Research

Article submitted to journal

Subject Areas:
Mechanics, Analysis, Civil Engineering

Keywords:
Inclusion-Based Boundary Element Method (iBEM), Bi-material Fundamental Solution, Equivalent Inclusion Method, Homogenization, Cross-Scale Material Modeling

Author for correspondence:
Liangliang Zhang, Huiming Yin
e-mail: llzhang@cau.edu.cn, yin@civil.columbia.edu

Effect of defects and reinforcements on the mechanical behavior of a bi-layered panel

C.L. Wu[2], L.L. Zhang [1] ,and H.M. Yin[2]

[1]Department of Applied Mechanics, China Agricultural University, 301 Yifu Building 17 Qinghua East Road, Beijing, 100083
[2]Department of Civil Engineering and Engineering Mechanics, Columbia University, 610 Seeley W. Mudd 500 West 120th Street, New York, 10027

This paper investigates the mechanical behavior of a bi-layered panel containing many particles in one layer and demonstrates the size effect of particles on the deflection. The inclusion-based boundary element method (iBEM) considers a fully bounded bi-material system. The fundamental solution for two jointed half spaces has been used to acquire elastic fields resulting from source fields over inclusions and boundary-avoiding multi-domain integral along the interface. Eshelby's equivalent inclusion method (EIM) is used to simulate the material mismatch with a continuously distributed eigenstrain field over the equivalent inclusion. The eigenstrain is expanded at the center of the inclusion, which provides tailorable accuracy based on the order of the polynomial of the eigenstrain. As a single-domain approach, the iBEM algorithm is particularly suitable for conducting virtual experiments of bi-layered composites with many defects or reinforcements for both local analysis and homogenization purposes. The maximum deflection of solar panel coupons is studied under uniform vertical loading merged with inhomogeneities of different material properties, dimensions, and volume fractions. The size of defects or reinforcements plays a significant role in the deflection of the panel, even with the same volume fraction, as the substrate is relatively thin.

THE ROYAL SOCIETY PUBLISHING

1. Introduction

Considering an ellipsoidal inhomogeneity embedded in an infinite homogeneous space under uniform far-field loading, Eshelby [1,2] proposed the equivalent inclusion method (EIM) to determine the elastic fields. Rather than directly solving the boundary value problems of multiple domains, the EIM treats the material in subdomains the same as the matrix by introducing a continuously distributed inelastic strain named eigenstrain [3], to simulate the material mismatch. Subsequently, by using EIM, the elastic fields of the initial problem can be acquired through the superposition of original fields caused by uniform far-field loading and disturbed fields induced by the eigenstrain. Thanks to Dyson's work [4] on the explicit domain integrals of ellipsoidal variable density functions, the EIM is intensively and widely applied in micromechanics to study both local fields and spatially-averaged fields (effective mechanical behaviors).

By using EIM in the evaluation of effective properties of composites under different assumptions, various micro-mechanical models [5] have been proposed, such as self-consistent scheme [6] and Halpin–Tsai model [7] with the assumption of the same average strain/stress on the single inhomogeneity and matrix. In addition, Mori-Tanaka [8] model and its modified versions [9] have been applied to investigate specific problems as porous ceramics, elastoplasticity and shape memory alloy polymers [10–12], etc. Although the above homogenization schemes have considered the inhomogeneity interactions, they are based on a strong assumption of infinite space, which is not realistic for either experimental specimens or industrial applications. When inhomogeneities are embedded in a finite domain, the boundary/interface effects are observed in the local fields [13] but have not been directly taken into account in micro-mechanical models. As one typical example, the interface effect [14] causes the angle shift of maximum principal stress of an embedded micro void. For multiple inhomogeneities problems, Yang et al. [10] found that homogeneously distributed inhomogeneities lead to maximum effective properties. Verified with virtual experiments [15] with the adequate number of inhomogeneities, the effective elastic constants of the composite gradually converge to a constant value statistically.

Due to the constraints on conventional homogenization models and their extensions, the concept of representative volume element (RVE) or unit cell (UC) was proposed, a structurally completely typical of the entire sample on average. According to Hill's definition [16], for a composite sample, the RVE should contain sufficient microstructural details to adequately represent the composites. Some efforts have been devoted to quantify the minimum dimensions of RVE [17]: (i) Kanit et al. [18] applied a statistical approach to determine dimensions of RVEs based on desirable precision and deduction with $4-5$ realizations; (ii) Terada et al. [19] presented the variational formulae for homogenization and employed the convergence of several macro and micro parameters, i.e. stresses in inhomogeneity, to reduce the dimension of an adequately large RVE. (iii) Gusev [20] applied the Monte Carlo algorithm to generate a statistically independent composite sample with $8, 25$ and 64 identical spheres. Dirrenberger et al. [21] concluded that slower convergence rate results in larger RVEs. In the above literature review, finite element method (FEM) and its extensions are intensively applied to solve the RVE with periodic boundary conditions as well as other numerical methods, such as EIM [22,23], finite volume method (FVM) [24], and boundary element method (BEM) [25].

Pioneers have proposed various numerical methods to investigate the mechanical behavior of bi-layered systems. Zhou et al. [26] investigated the effect of the hard coatings over substrate embedded with cuboid inhomogeneities, where the external loads are normal tractions and friction forces. To avoid inconsistency between the coating layer and the substrate, the authors [26] proposed to discretize the coating layer, inhomogeneities, and particularly assumed constant eigenstrain in each small "element". Subsequently, Dong et al. [27] utilized the same semi-analytical method and applied the linear approximation of dislocation density to investigate the plane strain fretting contact problems with vertical cracks. Among recent works, stress intensity factor (SIF) is a popular topic, where extensions of FEM are widely applied. Treifi and Oyadiji [28,29] developed a fractal-like FEM with displacement interpolation functions. The extended

FEM (XFEM) is implemented with crack-tip enrichment functions for cracks terminating at the bi-material interface [30]; and the mesh-free Galerkin method was applied to the crack interaction problems [31]. In addition, other numerical models, such as fast multi-pole BEM [32] and FEM/BEM with isogeometric analysis [33,34], have been reviewed [35,36]. Although the above methods can improve the accuracy with a discretization scheme, the solutions greatly rely on mesh quality near the bi-material interface, where singularity issues arise. To simplify the preparation process, Yue's group used the generalized Kelvin's solution [37] and extended it to n-layered solids [38,39] through the boundary element method, which analytically handles the continuity conditions between layers. Comparing the BEM with the classic Kelvin's solution, the recent studies from Yue's group [40,41] took advantage of the new fundamental solutions, in which the bi-layered material is treated as a single domain without mesh on the interface, but the integral form solution led to numerical integral with additional computational costs.

For a bi-material system, Walpole [42] provided an explicit form of fundamental solution, which can be used in the inclusion-based boundary element method (iBEM) [36] by significantly reducing the degree of freedoms (DOFs) in virtual experiments of composites. Wu et al. [43] also extended the iBEM for a single domain elastic analysis of bi-materials. Thanks to the explicit fundamental solution, the material mismatch between inhomogeneities and two matrices can be simulated with a continuously distributed eigenstrain field without any domain discretization. Following Mura's work [3], the continuous eigenstrain is expanded at the center of each inhomogeneity by the Taylor series, whose accuracy is tailorable by using uniform, linear or quadratic polynomial of eigenstrain based on the variation of the local field and desirable accuracy.

Recently, we [43] proposed single-domain boundary integral equations (BIEs) based on Walpole's solution, which mathematically considers continuity equations at the bi-material interface. Subsequently, thanks to analytical domain integrals with polynomial-form eigenstrain over spheres, Wu et al. [14] applied iBEM to investigate intensive bi-material interfacial effects on a single micro air void. This paper adopted iBEM in virtual experiments of a particulate composite for large-scale simulation with over $10,000$ inhomogeneities for structural response under different loading conditions, which discloses a new size effect of particles that is often ignored in other multiscale modeling.

Conventional homogenization models mainly use a large RVE under a uniform load to obtain the effective elastic moduli for modeling the structural behavior of a particulate composite. However, the accuracy of such a method on layered composites is significantly jeopardized, as it ignores the two essential issues. The first is that the bending of the panel results in a linear variation of elastic fields, while the homogenization model only handles the cause of uniform loads. And the other is that the size of RVE is constrained by the thickness of layers, which is challenging to find a convergent effective stiffness with the particle size and the layer thickness. Consequently, the size effects of particles produce more contribution to the overall structural behavior. Without the mesh of particle surfaces or the interface of bi-layered materials, the new method creates an opportunity for cross-scale modeling of composites, particularly when the size of inhomogeneities is not adequately small compared to the structural dimension.

In the following, Section 2 states the problem of a heterogeneous material system with several subdomains. Subsequently, the fundamental solution of two-jointed dissimilar half spaces under one concentrated loading, explicit domain integrals over spherical subdomain and global matrix of iBEM are proposed in Section 3. Section 4 validates the aforementioned iBEM algorithm by the finite element method (FEM) by comparing the neighboring elastic fields around inhomogeneities, where the results by uniform, linear and quadratic orders of eigenstrain are discussed for different levels of particle-boundary interactions.Section 5 investigates the maximum deflection of a BIPV panel under uniform vertical loading with various material properties, dimensions, and volume fractions of inhomogeneities. In Section 6, interesting microstructure effects on the accuracy of elastic fields are present with the help of virtual

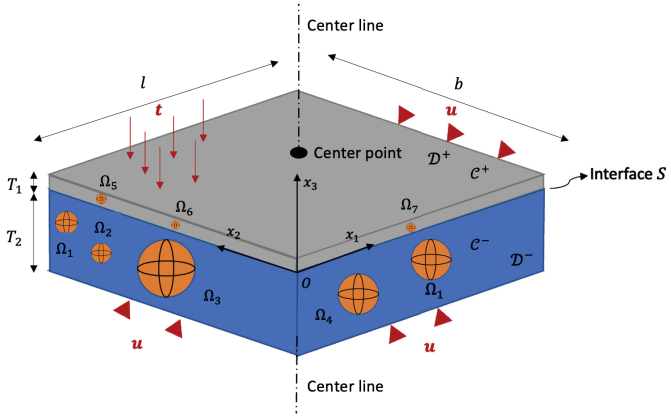

Figure 1: Schematic plot of a bi-layered system $\mathcal{D}$ composed of two matrix $\mathcal{D}^{\pm}$ and multiple N_I subdomains Ω_I subjected to prescribed boundary conditions

experiments of homogenization of an individual layer of the bi-material system. Finally, some conclusive remarks are presented.

2. Problem Statement

Consider a bi-layered domain $\mathcal{D}$ composed of multiple N_I inhomogeneities Ω^I in two-jointed isotropic dissimilar layers, the upper $\mathcal{D}^+$ and the lower $\mathcal{D}^-$. Here the inhomogeneities can be located either in the upper or lower matrix layers but not across their interface for simplicity. Actually, in the application of the BIPV panel, only the substrate exhibits inhomogeneities. The bi-layered domain $\mathcal{D}$ can be written as a union of two matrices and the subdomains of the inhomogeneities, $\mathcal{D}^+ \bigcup \mathcal{D}^- \bigcup_{N_I} \Omega^I$. In general, the two layers and subdomains exhibit different material properties ,and the stiffness tensor can be expressed as $\mathcal{C}^m_{ijkl}$, where $m = +, -$ (two matrices) or $m = 1, 2, \ldots, N_I$ (subdomains). Taking the upper layer $\mathcal{D}^+$ for example, the stiffness tensor $\mathcal{C}^+ = \lambda^+ \delta_{ij}\delta_{kl} + \mu^+(\delta_{ik}\delta_{jl} + \delta_{il}\delta_{jk})$, where λ^+ and μ^+ are the lamé parameters of the upper layer. Without the loss of any generality, the bi-material interface S is selected as $x_1 - x_2$ plane when $x_3 = 0$, and cases with inclined interfaces can be solved with coordinate transformation.

Shown in Fig.1, the dimensions and boundary conditions of the bi-layered system are given as: (i) T_1 and T_2 are the thickness of $\mathcal{D}^+$ and $\mathcal{D}^-$, respectively; (ii) l and b denote length and width of cuboid layers; (iii) $\mathcal{D}$ is subjected to prescribed boundary conditions, where **t** and **u** stand for traction and displacement boundaries, respectively. In the following, we assume that the interfaces between two layers $\mathcal{D}^+$, $\mathcal{D}^-$ and subdomains are perfectly bonded, where the continuity equations of displacements and traction are satisfied as Eq. (2.1),

$$u_i(\mathbf{x}^+) = u_i(\mathbf{x}^-), \quad \sigma_{ij}(\mathbf{x}^+)n_j(\mathbf{x}^+) = \sigma_{ij}(\mathbf{x}^-)n_j(\mathbf{x}^-) \tag{2.1}$$

where **n** represents the unit normal vector of inhomogeneity interfaces $\partial\Omega^I$ or bi-material interface S; the superscripts "+" and "-" means the inward and outward sides of the interfaces. Combining the continuity equations on interfaces as Eq.(2.1) with prescribed boundary conditions, a boundary value problem is well-posed, which can be numerically solved using the multi-region schemes. Due to the existence of bi-material interface S, stress discontinuities and shear stress singularities arise, which generally require more computational resources. In addition, besides the ellipsoidal inhomogeneities, the particle interactions and its interaction with the interface or boundary may produce significant disturbance to the local elastic field. In this

paper, alternatively, the iBEM algorithm mathematically considers bi-material interface S and simulates material mismatch through continuous eigenstrain fields ε^I_{ij} on each subdomain Ω^I, which simplifies the pre-processing and saves computational resources.

3. Formulation

(a) Fundamental Solution of Two Jointed Half Spaces

Considering a two-jointed homogeneous dissimilar half spaces $\mathcal{D}$ with interface $x_1 - x_2$, Walpole [42] firstly proposed the fundamental solution of a concentrated loading, when the excitation (source) is located in upper phase $\mathcal{D}^+$. The fundamental solution is composed of two parts, the infinite and image parts, where the infinite part is also known as the Kelvin's solution. Due to the existence of image part, the fundamental solution changes accordingly whether source point $\mathbf{x}'$ and field point $\mathbf{x}$ are in the same material phase. Wu et al. [43] complete the fundamental solution through the method of symmetry,

(a) When $x_3' x_3 \geq 0$, the source and field points are in the same material phase, and

$$\begin{aligned} 4\pi\mu^w G^y_{ij}(\mathbf{x},\mathbf{x}') = &(\delta_{ij}\phi - \frac{\psi_{,ij}}{4(1-\nu^w)}) + A^y\overline{\phi}\delta_{ij} + \chi B^y(\delta_{i3}\delta_{jk} - \delta_{ik}\delta_{j3})\overline{\alpha}^y_{,k} \\ &- C^y x_3\left[Q_J\overline{\psi}_{,ij3} + 4(1-\nu^w)\delta_{j3}\overline{\phi}_{,i} + 2(1-2\nu')\delta_{i3}Q_J\overline{\phi}_{,j} - Q_J x_3\overline{\phi}_{,ij}\right] \\ &- D^y Q_I Q_J\overline{\psi}_{,ji} - (G^y + B^y)Q_J\overline{\beta}^y_{,ij} \end{aligned} \tag{3.1}$$

(b) When $x_3' x_3 < 0$,the source and field points are not in the same material phase, and

$$\begin{aligned} 4\pi\mu^w G^y_{ij}(\mathbf{x},\mathbf{x}') = &(\delta_{ij}\phi - \frac{\psi_{,ij}}{4(1-\nu^w)}) + A^y\phi\delta_{ij} + \chi B^y(\delta_{i3}\delta_{jk} - \delta_{ik}\delta_{j3})\alpha^y_{,k} \\ &- D^y\psi_{,ij} - \chi x_3 F^y\alpha^y_{,ij} - (G^y + B^y)Q_I\beta^y_{,ji} \end{aligned} \tag{3.2}$$

where $\psi = |\mathbf{x}' - \mathbf{x}|$ is the biharmonic potential and $\phi = \psi^{-1}$ is its reciprocal or the Newton potential; the first two terms in the parenthesis come from the Kelvin's solution for infinite space; the superscript $\overline{(.)}$ represent image source points, for instance, $\overline{\psi} = |\mathbf{x} - \overline{\mathbf{x}'}|$ and $\overline{\mathbf{x}'} = (x_1', x_2', -x_3')$; $\mathbf{Q} = (1, 1, -1)$ handles the partial derivatives of image part through the bi-material interface S and the dummy index notations does not work for capitalized subscripts, i.e Q_I; the coefficient χ and superscripts w, y differs when source point $x_3' \geq 0$ ($\chi = 1, w = +$ and $y = u$) and $x_3' < 0$ ($\chi = -1, w = -$ and $y = l$); coefficients $A^u \ldots G^u$ are material constants associated with $\mathcal{D}^+$ as;

$$\begin{aligned} A^u &= \frac{\mu^+ - \mu^-}{\mu^+ + \mu^-}, \quad B^u = \frac{2\mu^+(1-2\nu^+)(\mu^+ - \mu^-)}{(\mu^+ + \mu^-)(\mu^+ + \mu^-(3-4\nu^+))} \\ C^u &= \frac{\mu^+ - \mu^-}{2(1-\nu^+)(\mu^+ + (3-4\nu^+)\mu^-)}, \quad D^u = \frac{3-4\nu^+}{2}C^u \\ F^u &= \frac{2\mu^+(\mu^+(1-2\nu^-) - \mu^-(1-2\nu^+))}{(\mu^+ + \mu^-(3-4\nu^+))(\mu^- + \mu^+(3-4\nu^-))} \\ G^u &= \frac{\mu^+(\mu^-(1-2\nu^-)(3-4\nu^+) - \mu^+(1-2\nu^+)(3-4\nu^-))}{(\mu^+ + \mu^-(3-4\nu^+))(\mu^- + \mu^+(3-4\nu^-))} \end{aligned} \tag{3.3}$$

The coefficients $A^l - G^l$ related to the lower phase $\mathcal{D}^-$, can be obtained through interchanging sequences of material constants, for instance, $A^l = \frac{\mu^- - \mu^+}{\mu^- + \mu^+}$. In general, two domains $\mathcal{D}^+$ and $\mathcal{D}^-$ exhibit different material properties. When the material properties are the same in each domain, the fundamental solution reduces to the Kelvin's solution as all coefficients $A, B, \cdots, G$ yield

zeros. Components in the fundamental solution other than ψ and ϕ are provided below,

$$\begin{aligned} \alpha^u &= \ln[x_3' - x_3 + \psi], \quad \overline{\alpha}^u = \ln[x_3' + x_3 + \overline{\psi}] \\ \beta^u &= (x_3' - x_3)\alpha^u - \psi, \quad \overline{\beta}^u = (x_3' + x_3)\overline{\alpha}^u - \overline{\psi} \\ \alpha^l &= \ln[-x_3' + x_3 + \psi], \quad \overline{\alpha}^l = \ln[-x_3' - x_3 + \overline{\psi}] \\ \beta^l &= (-x_3' + x_3)\alpha^l - \psi, \quad \overline{\beta}^l = (-x_3' - x_3)\overline{\alpha}^l - \overline{\psi} \end{aligned} \tag{3.4}$$

where 4 branches of α and β can be rewritten as a finite part of the definite integral with respect to x_3, such that $\alpha^u = \int_{x_3}^{-\infty} \phi(x_1, x_2, t)\, dt$, which are also called Boussinesq's displacement potentials [44]. Other branches of α and β are elaborated in Section 1 of the Supplementary Information. In the literature, several special cases of the bi-material fundamental solutions were investigated and proposed, such as (i) bi-material Stokes flow with incompressive assumptions of Poisson's ratio 0.5; (ii) Lorentz's, Mindlin's, and Boussinesq's solution of semi-infinite spaces with concentrated loadings, which assumes zero stiffness of one material phase [36].

(b) Inhomogeneities in an Infinite Two-jointed Dissimilar Half Spaces

In Section 2, the boundary value problem is illustrated that a finite domain composed of two layers $\mathcal{D}^{\pm}$ embedded with multiple inhomogeneities. For a linear elastic problem, the entire elastic fields can be obtained through the superposition of each subdomain. In this subsection, we first consider an infinite space $\mathcal{D}$ composed of two jointed dissimilar half spaces $\mathcal{D}^{\pm}$ and one embedded subdomain Ω_I with an inhomogeneity, which can be replaced by an eigenstrain ε_{ij}^{I*}. Although in Eshelby's celebrated problems [1,2] for ellipsoidal inhomgeneity, the eigenstrain field is uniformly distributed, subsequent work by Mura [3] proposed to use polynomial-form eigenstrain field under interactions of inhomogeneities and boundary effects [15]. Following Mura's notation, the eigenstrain in subdomain Ω_I can be written as a Taylor series polynomial in Eq.(3.5),

$$\varepsilon_{ij}^{I*} = \varepsilon_{ij}^{I0*} + \varepsilon_{ijp}^{I1*}(x_p' - x_p^{Ic}) + \varepsilon_{ijpq}^{I2*}(x_p' - x_p^{Ic})(x_q' - x_q^{Ic}) + \dots \tag{3.5}$$

where superscripts $0, 1$ and 2 represent uniform, linear and quadratic order of eigenstrains; $\mathbf{x}^{Ic}$ is the center of I^{th} subdomain. Notice that although eigenstrain can be expanded to higher orders, in this paper, we only consider up to quadratic term, which can provide high-fidelity results in most cases. The disturbed displacement field caused by eigenstrains ε_{ij}^{I*} can be obtained through domain integral of fundamental solution in Eqs.(2) and (3),

$$u_i(\mathbf{x}) = \int_{\Omega_I} \frac{\partial G_{ij}(\mathbf{x}, \mathbf{x}')}{\partial x_m'} \varepsilon_{kl}^*(\mathbf{x}') \mathcal{C}_{jmkl}(\mathbf{x}')\, dV(\mathbf{x}') = \sum_{I=1}^{N_I} \left\{ g_{ikl}\varepsilon_{kl}^{I0*} + g_{iklp}\varepsilon_{klp}^{I1*} + g_{iklpq}\varepsilon_{klpq}^{I2*} \right\} \tag{3.6}$$

$$\varepsilon_{ij}(\mathbf{x}) = \sum_{I=1}^{N_I} \left\{ S_{ijkl}\varepsilon_{kl}^{I0*} + S_{ijklp}\varepsilon_{klp}^{I1*} + S_{ijklpq}\varepsilon_{klpq}^{I2*} \right\} \tag{3.7}$$

where N_I is the number of subdomains; $g_{iklp\dots} = \int_{\Omega} G_{ij,m'} \mathcal{C}_{jmkl}(x_p' - x_p^{Ic}) dV(\mathbf{x}')$ and $S_{ijklp\dots} = \frac{g_{iklp\dots,j} + g_{jklp\dots,i}}{2}$ are Eshelby's tensors for displacement and strain, respectively; the explicit expressions for domain integrals of fundamental solutions are provided in Section 1 of Supplementary Information.

(c) Inhomogeneities in a Finite Two-jointed Dissimilar Half Spaces

In Section 3.2, through the technique of fundamental solution, the disturbed elastic fields by one inhomogeneity was derived as Eqs.(3.6) and (3.7). Superposing with boundary responses,

the displacement at field point **x** can be written as a combination of BIEs and disturbance by eigenstrain (i.e., quadratic order) as Eq.(3.8),

$$\begin{aligned} u_i(\mathbf{x}) &= -\int_{\partial\mathcal{D}^t} T_{ij}(\mathbf{x},\mathbf{x}')u_j(\mathbf{x}')d\mathbf{x}' + \int_{\partial\mathcal{D}^u} G_{ij}(\mathbf{x},\mathbf{x}')t_j(\mathbf{x}')d\mathbf{x}' + \int_{\Omega_I} \frac{\partial G_{ij}(\mathbf{x},\mathbf{x}')}{\partial x'_m}\varepsilon^*_{kl}(\mathbf{x}')C_{jmkl}(\mathbf{x}')\,dV(\mathbf{x}') \\ &= -\sum_{e=1}^{NE} H_{ij}u^e_j + \sum_{e=1}^{NE} U_{ij}t^e_j + \sum_{I=1}^{N_I}\left\{g_{ikl}\varepsilon^{I0*}_{kl} + g_{iklp}\varepsilon^{I1*}_{klp} + g_{iklpq}\varepsilon^{I2*}_{klpq}\right\} \end{aligned} \tag{3.8}$$

where G_{ij} is the fundamental solution of displacement in Eqs.(2) and (3). Derived from G_{ij}, $T_{ij} = \frac{C_{imkl}(\mathbf{x}')(G_{kj,l'}+G_{lj,k'})}{2}n_m(\mathbf{x}')$ is fundamental solution of traction. In order to solve the problem numerically, the mesh on the boundary enables the discretization of boundary responses, where displacement and traction can be written as nodal values multiplied by shape functions. In Eq.(3.8), $H_{ij} = \int_{S_e} T_{mi}(\mathbf{x},\mathbf{x}')N_{mj}(\mathbf{x}')\,dS$ and $U_{ij} = \int_{S_e} U_{mi}(\mathbf{x},\mathbf{x}')N_{mj}(\mathbf{x}')\,dS$ are coefficients for displacement and traction, respectively. The superscript e stands for nodal quantities within e^{th} boundary element and NE represents the number of boundary elements. The interactions between inhomogeneities and boundaries are involved through equations of displacement and traction of BEM. As Eqs.(2) and (3) take interfacial continuity conditions into account, the boundary mesh is the same as homogeneous solids ,and no elements are needed along the interface at $x_3 = 0$.

Subsequently, through the compatibility equation, the strain field at point **x** can be obtained as

$$\varepsilon_{ij}(\mathbf{x}) = -\sum_{e=1}^{NE} H_{im,j}u^e_m + \sum_{e=1}^{NE} U_{im,j}t^e_m + \sum_{I=1}^{N_I}\left\{S_{ijkl}\varepsilon^{I0*}_{kl} + S_{ijklp}\varepsilon^{I1*}_{klp} + S_{ijklpq}\varepsilon^{I2*}_{klpq}\right\} \tag{3.9}$$

In Eq.(3.5), the eigenstrain is written in the polynomial form. Shown in Eq.(3.10), for uniform, linear and quadratic orders of eigenstrain, 6, 18, and 60 more stress equivalent equations are required for each inhomogeneity as follows

$$\begin{aligned} \mathcal{C}^w_{ijkl}(\varepsilon^b_{kl} + \varepsilon'_{kl} - \varepsilon^{I0*}_{kl}) &= \mathcal{C}^I_{ijkl}(\varepsilon^b_{kl} + \varepsilon'_{kl}) \\ \mathcal{C}^w_{ijkl}(\varepsilon^b_{kl,m} + \varepsilon'_{kl,m} - \varepsilon^{I1*}_{klm}) &= \mathcal{C}^I_{ijkl}(\varepsilon^b_{kl,m} + \varepsilon'_{kl,m}) \\ \frac{1}{2!}\mathcal{C}^w_{ijkl}(\varepsilon^b_{kl,mn} + \varepsilon'_{kl,mn} - 2\varepsilon^{I2*}_{klmn}) &= \frac{1}{2!}\mathcal{C}^I_{ijkl}(\varepsilon^b_{kl,mn} + \varepsilon'_{kl,mn}) \end{aligned} \tag{3.10}$$

Since the inhomogeneity may be located in either $\mathcal{D}^+$ or $\mathcal{D}^-$, $w =$ "+" when $x^{Ic}_3 > 0$ and $w =$"-" when $x^{Ic}_3 < 0$; ε^b_{ij} represents strain by BIEs in Eq.(3.9); ε'_{ij} is disturbed strain by polynomial-form eigenstrain as Eq.(3.7). Hence, the interactions between inhomogeneities are considered such that Eq.(3.7) contains disturbance from all inhomogeneities. Assembling the BIEs of conventional BEM, boundary interactions, and stress equivalent conditions, the global matrix of iBEM can be constructed [36]. Solving the system of linear equations, we can acquire both boundary responses and eigenstrain fields on each inhomogeneity; therefore, the elastic fields can be obtained through Eqs.(3.8) and (3.9).

4. Numerical Verification of iBEM with Bi-material Fundamental Solution

Although layered panels with defects or reinforcements are widely used in engineering applications, physical experiments and characterization of the size effects of the defects and reinforcements are time consuming and expensive. The present iBEM algorithm provides an excellent tool for virtual experiments on computers. As no experimental data is available to validate of the iBEM code, the well-established finite element method (FEM) will be used for verification through comparisons of neighbor elastic fields around inhomogeneities by both

iBEM and FEM methods. When iBEM is verified to be a high-fidelity numerical method, we can use it for large scale virtual experiments that FEM may not be applicable. In this section, 10-node quadratic tetrahedral elements are applied for consistency, and a transition-zone mesh is employed to reduce computational costs in finite element analysis, which is elaborated in Section 2 of Supplementary Information.

Because of the disturbance induced both by inhomogeneities interactions and boundary/interface effects, Eshelby's solution of uniformly distributed eigenstrain cannot satisfy the stress equivalent condition for all points in the equivalent inclusion. Therefore, the eigenstrains are expressed as polynomials expanded at the center of each subdomain. In order to illustrate how solutions with different orders of polynomial-form eigenstrain perform with uniform, linear and quadratic terms, the numerical case studies are investigated considering both inhomogeneity interactions and interface effects. In Eq.(3.10), the equivalent stress conditions rely on the domain integral of subdomains (shown in Supplementary Information), which is mainly dependent on the distance ratio $d = h/a$ between the distance of two inhomogeneities (h) and the radius (a) of the inhomogeneities. Consequently, a smaller distance ratio suggests more intensive inhomogeneity interactions and vice versa. Regarding the interface effects, specifically in this paper, its intensity is judged by the ratio between the distance to the interface and the radius a. For a bi-material system, if the inhomogeneity is far from the interface S, the image terms in fundamental solution vanishes rapidly, providing negligible disturbances. Consequently, the elastic fields reduce to Eshelby's solution in an infinite space.

As indicated in Fig.1, the prescribed boundary conditions are, (i) uniform downward surface traction $T = (0, 0, -100)$ MPa applied on the top surface of $\mathcal{D}^+$; (ii) displacement constrained ($u = (0, 0, 0)$) bottom surface of $\mathcal{D}^-$; (iii) all other 4 surfaces are free of traction. The width b, length l and thickness T_1, T_2 are all selected as 1 m. Regarding material properties, without the loss of any generality, let the upper phase $\mathcal{D}^+$ and the lower phase $\mathcal{D}^-$ be glass ($\mu^+ = 30$ GPa, $\nu^+ = 0.2$) and concrete ($\mu^- = 15$ GPa, $\nu^- = 0.2$), respectively. Two material properties are chosen for parametric studies of the inhomogeneity as the softer $\mu^I = 10$ GPa, $\nu^I = 0.3$ and the stiffer $\mu^I = 60$ GPa and $\nu^I = 0.3$. For 3D surface mesh, $1,000$ 4-node quadrilateral boundary elements are used.

(a) Interface effects on One Inhomogeneity

Since the influence of source fields, eigenstrain, is calculated through domain integrals of the bi-material Green's function, the perturbed elastic fields and interfacial effects are mainly related to the ratio of distances between the center of inhomogeneity and field points. In such case, the observation of local mechanical properties by one spherical inhomogeneity remains the same under a dimensionless coordinate defined by distance and radius a of the inhomogeneity. Considering the computational costs and numerical convergence in FEM, the radius a is assumed as 0.1 m, and the elastic fields are presented in dimensionless coordinates $x_1/a, x_3/a$. Indicated in Fig.2, a single softer / stiffer inhomogeneity is placed along the center line with a distance $1.1a$ to the interface S. To verify the iBEM results, an FEM model is constructed with the number of elements and nodes at $1,508,038$ and $2,394,773$, respectively. Comparing the displacement curves in Fig. 2(a) and Fig.2(b), the results of iBEM with uniform, linear and quadratic order eigenstrains agree well with that of FEM. Because of the material difference between two layers, the slope of displacement u_3 alters at the interface S; due to the disturbance by the inhomogeneity, the slope decreases for stiffer case and vice versa. Regarding normal stresses, certain discrepancies are observed between all curves of iBEM and FEM, where the quadratic case provides the best prediction with an error less than 1%. In Eqs. (3.1) and (3.2), the image terms become dominant as the distance to interface decreases, producing a more complicated elastic field. Still, the uniform eigenstrain assumption provides feasible and accurate analysis (with tolerance) for 1^{st} order partial differentiated terms, which is useful for the homogenization of effective properties as functions of displacements and known pressure. However, for investigation on 2^{nd} order partial

differentiated terms, i.e local stresses, it is essential to consider quadratic eigenstrain, similar to the boundary effects for semi-infinite domain [15].

Shown in Fig.3, when the distance ratio h/a is 2, the interface effects reduce rapidly. It is noted that the distribution of stresses within the inhomogeneity becomes more flattened, and the variation is smaller. Comparing the case of distance ratio 1.1, linear order eigenstrain could provide fairly good results, which indicates a smaller variation of eigenstrain over the inhomogeneity. Subsequently, when the distance ratio increases, the elastic field gradually becomes similar to Eshelby's solution with a uniform eigenstrain.

(b) Inhomogeneity Interactions with Side-side and Top-down Alignments

In order to verify the algorithm for inhomogeneity interaction, two cases of inhomogeneity alignment are considered: (i) side-by-side and (ii) top-down. In case (i), the two spherical softer/stiffer inhomogeneities with radius $a = 0.1$ m are placed at height $h = 0.15$ m in the upper layer $\mathcal{D}^+$ along the horizontal center line and the distance between two centers are $2.2a$. Regarding case (ii), to retain interface effects, the two spherical softer/stiffer inhomogeneities with radius $a = 0.1$ m are placed at the height $a = 0.11$ m in both layers along the vertical center line and thus the distance between the two centers are $2.2a$ as well. In FEM, $4,606,274$ nodes and $3,440,291$ elements are applied. Shown in Fig.4, similar to the previous section, iBEM with three orders of accuracy are compared with FEM on variation of normal stresses along the horizontal and vertical center lines. It is observed that curves "iBEM-Uniform-σ_{11}" exhibit the largest discrepancies in comparison with FEM, while linear and quadratic accuracy agree well with FEM. In Fig.4(c) and Fig.4(d), in the range $x_3 \in [0.1, 0.2]$ m, the linear results are smaller while the quadratic results are larger than that of FEM, which can be interpreted as polynomial approximation of true eigenstrain field. In general, higher order polynomials, such as variational method, can provide more accurate prediction. However, considering compromise of computational costs and error tolerance, quadratic order is a rational choice. In addition, since the external loading is applied in x_3 direction, the primary attention should be paid on σ_{33} and iBEM with three orders of accuracy all agree well with the FEM results.

In Fig.5, with distance ratios 0.1 for interface and 2.2 for two centers, the top-down case involves intensive interface effects and inhomogeneities interactions. In FEM, $5,777,482$ nodes and $4,307,203$ elements are applied. In Fig.5(a), all six curves with iBEM agree well with FEM except some extreme points at the edge of the inhomogeneity. When the inhomogeneity become stiffer, the material mismatch increases, larger discrepancies are observed, while the quadratic case provides the closest to the FEM prediction among other orders.

5. Virtual experiments with BIPV test coupons

(a) The virtual experimental setup with the iBEM

The building integrated photovoltaic (BIPV) panels are usually installed at the roof, which can be simplified as a bi-material system composed of glass solar panel glued on a concrete substrate [45]. In general, the substrate of a BIPV panel is simply supported on two opposite edges during the construction [46]. Since the larger deflection of the panel is the control parameter in design, which causes visual impacts and photovoltaic cell cracking, it is critical to fully understand the deformation of the panel in both material and structural levels. As concrete substrate is a composite with microvoids and particulate reinforcements, although the concrete is generally homogenized into a uniform material with certain elastic constants, the size of the voids and particles may play a role in structural deformation.

To investigate the structural response of a panel with different material design, following Fig.1, virtual experiments are set up with test coupons as follows:

(i) the width b and length l are set as 0.1 m;

(ii) the thickness of the upper layer T_1 and the lower layer T_2 are 0.003 m and 0.005 m,

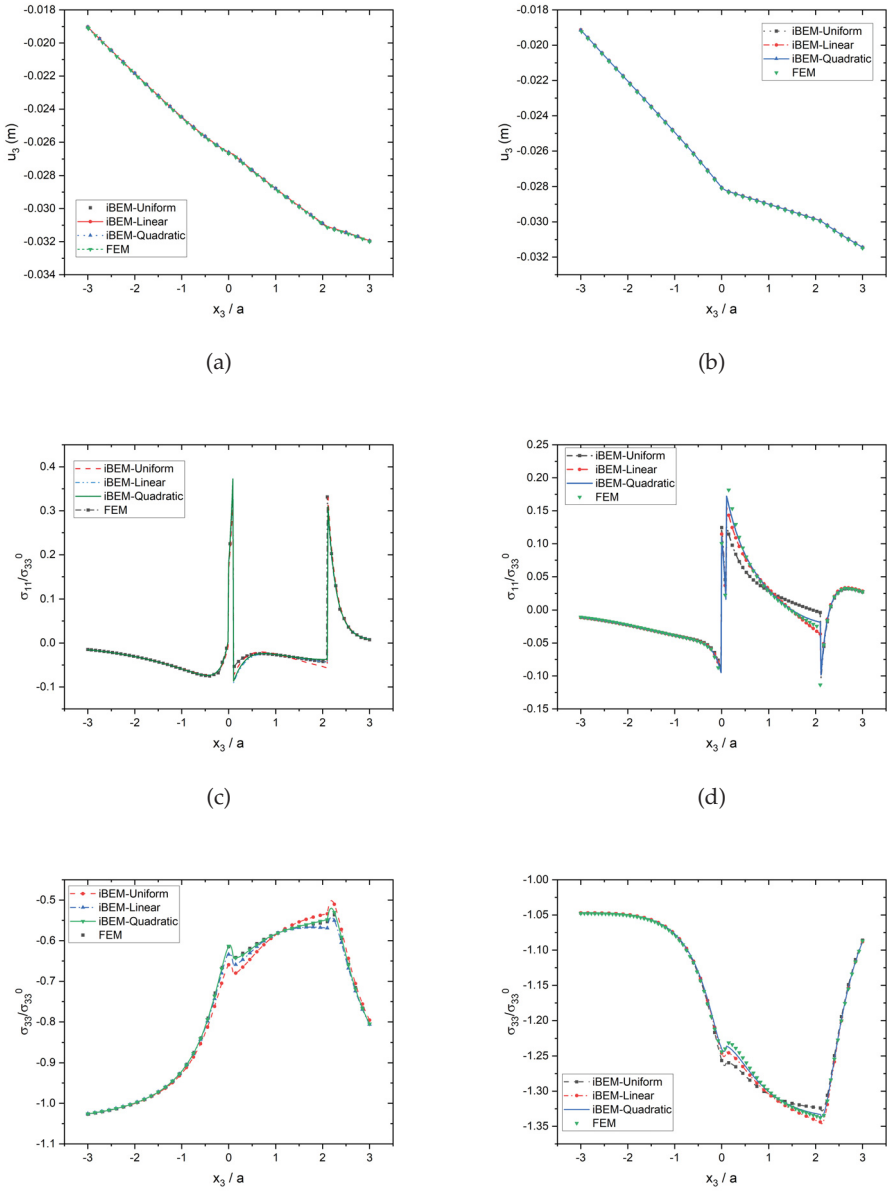

Figure 2: Variation of displacement u_3 for a (a) softer and (b) stiffer inhomogeneity, respectively; normal stress $\sigma_{11}/\sigma_{33}^0$ for a (c) softer and (d) stiffer inhomogeneity, respectively; normal stress $\sigma_{33}/\sigma_{33}^0$ for a (e) softer and (f) stiffer , respectively, along the vertical center line $x_3/a \in [-3, 3]$ under uniform downward pressure 100 MPa when $h/a = 1.1$

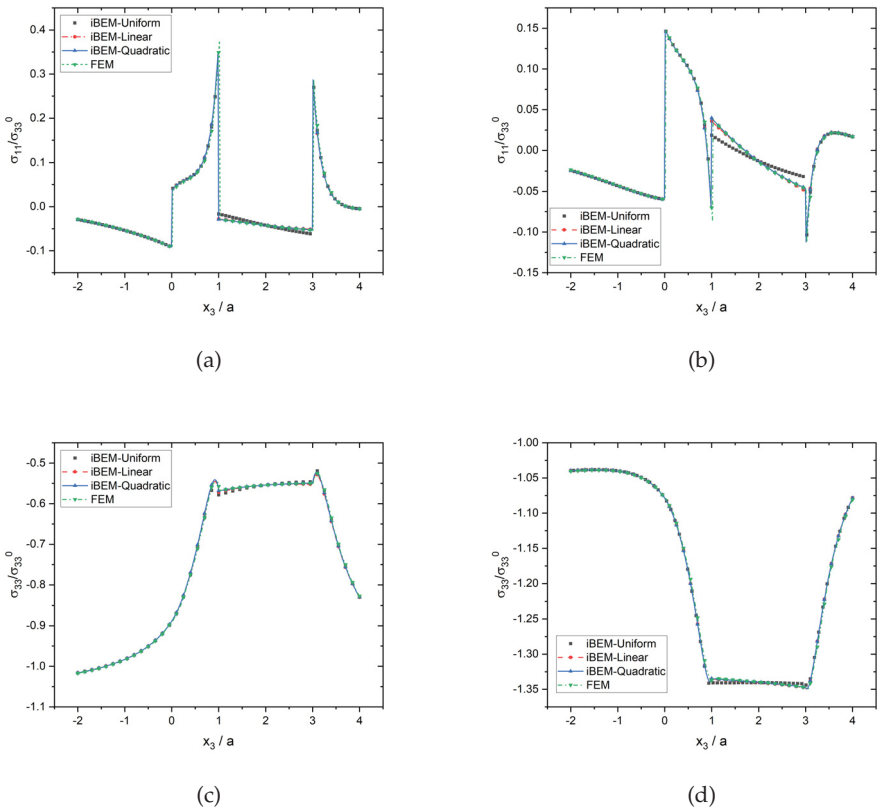

Figure 3: Variation of normal stress $\sigma_{11}/\sigma^0_{33}$ for a (a) softer and (b) stiffer inhomogeneity, respectively; normal stress $\sigma_{33}/\sigma^0_{33}$ for a (a) softer and (b) stiffer inhomogeneity, respectively along the vertical center line $x_3/a \in [-2, 4]$ under uniform downward pressure 100 MPa when $h/a = 2$

respectively.

The Robin's boundary condition of the BIPV coupons are as follows:

(i) uniform downward surface traction $T = (0, 0, -1)$ MPa applied on top surface of $\mathcal{D}^+$;

(ii) simply supported edge 1 $x_1 = 0$ and edge 2 $x_1 = 0.1$ m of the bottom surface of $\mathcal{D}^-$; specifically, displacements are constrained for edge 1 and only vertical displacement component is fixed for edge 2;

(iii) all other 4 surfaces are free of traction.

In the following, influence brought by 4 microstructural properties was investigated, the volume fraction, size variation, material properties and distribution of inhomogeneities.

Generally, given a prescribed volume fraction of inhomogeneities and their material properties, the homogenization schemes, such as RVE or micromechanical models, transforms the concrete composite into a uniform material and the BIPV coupon becomes a bi-material system with two homogeneous layers through applications of effective behaviors. In the following comparison, regarding micromechanical models, the Mori-Tanaka scheme is employed. As for numerical homogenization, effective elastic moduli are obtained with iBEM on a concrete specimen containing multiple inhomogeneities under standard uni-axial loading [15]. In Eq. (3.1) and Eq. (3.2), when material properties of two layers are the same $\mathcal{C}^+ = \mathcal{C}^-$, the fundamental

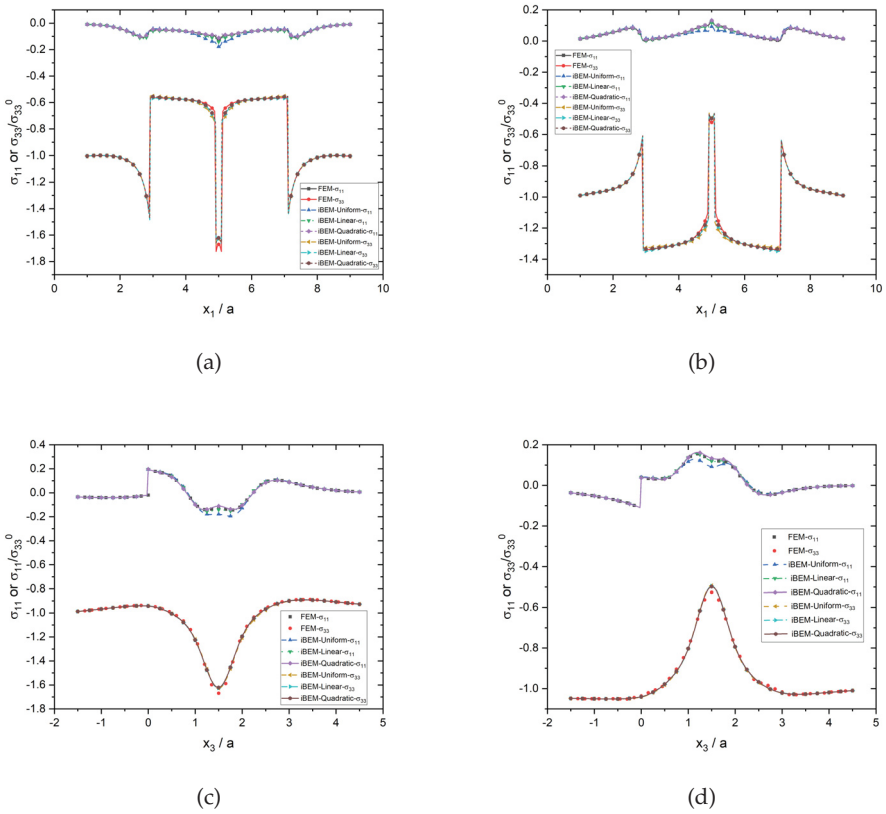

Figure 4: Comparison of normal stress variation between FEM and iBEM (three order of accuracy) on side-by-side interaction along horizontal center line $x_1/a \in [1, 9]$ for two (a) softer and (b) stiffer inhomogeneities, respectively; along vertical center line $x_3/a \in [-1.5, 4.5]$ for two (a) softer and (b) stiffer inhomogeneities, respectively under uniform downward pressure 100 MPa

solution reduce to Kelvin's solution, which can be applied on prediction of effective properties. Wu and Yin [15] showed that when the number of inhomogeneities is large enough, effective properties obtained from the uni-axial loading become convergent. Following the same fashion [15], (i) the effective Young's modulus is calculated by the applied pressure t_3^0 divided by the average vertical strain $\overline{\varepsilon_{33}}$; and (ii) the effective Poisson's ratio is obtained through the ratio of the average lateral strain in either x_1 or x_2 direction to the vertical strain $\overline{\varepsilon_{33}}$, where the averaged strains can be acquired as the ratio of the displacement to the original length.

As mentioned in Section 1, conventional micromechanics generally conducts homogenization of composites to obtain the effective stiffness, and the maximum deflections can be calculated through structural analysis with the analytical formulation using the effective stiffness. In such a case, only when two strong conditions of uniform load and adequately small inhomogeneities are satisfied, the prediction can be accurate with the existence of an RVE. However, when a panel is subjected to transverse loading, the stress caused by bending will be linear along the thickness while the thickness of a panel may not be large enough to form an RVE. Then the size effects of the inhomogeneity or panel thickness may be significant, which makes the formulation inaccurate or invalid.

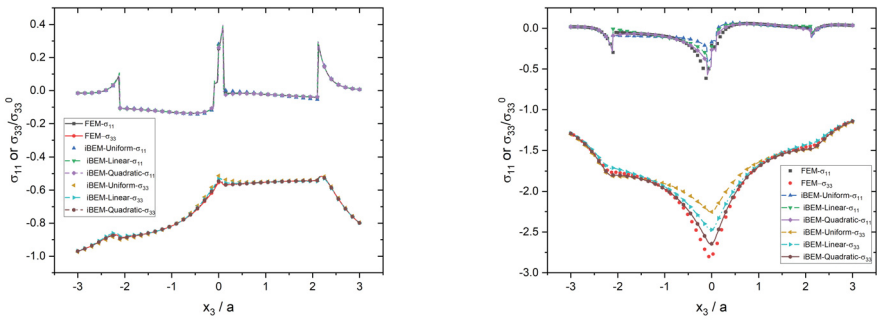

(a) (b)

Figure 5: Comparison of normal stress variation between FEM and iBEM (three order of accuracy) on top-down interaction along vertical center line $x_3/a \in [-3, 3]$ for two (a) softer and (b) stiffer inhomogeneities, respectively under uniform downward pressure 100 MPa

(b) Effects of different volume fractions

To reduce self weight, lightweight concrete (LWC) panels are widely applied as a substrate for a BIPV. In this section, the variations of deflection, especially the center and maximum ones, are investigated versus different volume fractions of air voids. In order to exclude effects brought by dimensions, the distribution and number of inhomogeneities, the bottom concrete panel $\mathcal{D}^-$ is evenly divided into $1 \times 20 \times 20$ cuboids, where 400 equal-sized spherical inhomogeneities are placed at the centers of cuboids. For volume fraction ranging from 5% to 40%, the radii of the inhomogeneities were adjusted accordingly $[1.143, 2.285]$ mm. As indicated as Fig.7, the deflections at the bottom surface of concrete panel $\mathcal{D}^-$ were plotted for homogeneous, 20% and 40% volume fraction, respectively. The contour plots used 101×101 uniformly distributed field points on the boundary, where the deflections are calculated through interpolations of nodal displacements. It is noted that the maximum deflection exists at the middle point of edges $(0.05, 0)$ or $(0.05, 0.1)$, which can be interpreted as free edge boundary conditions. As the volume fraction of air voids increases, the similar pattern / distribution of deflection retains, however, the maximum deflection becomes larger, from 0.0055 m to 0.00706 m. In general, softer inhomogeneities cause local stress concentration resulting in larger deformations. Similarly, more air voids also lead to a larger deflection of the panel. However, the classic micromechanics-based models predict the effective stiffness of composites varying with the volume fraction only [9], and the particle size effect is ignored by using a single particle in an infinite domain. Therefore, it is interesting to compare the above results with the one homogenizing the LWC panel as a uniform material.

As shown in Fig. 6, the effective properties of the bottom layer are calculated through iBEM and compared with three homogenization schemes, namely the Mori-Tanaka, Voigt, and Dilute models. The effective Young's modulus $\overline{E}$ by iBEM is between the curves of "Mori-Tanaka" and "Voigt". As a mixture rule, the Voigt model simply assumes the average strains on both matrix and inhomogeneity phases are the same and over estimates the elasticity. The Dilute scheme directly applies Esehlby's solution of one spherical inhomogeneity in full space, which does not consider interactions between inhomogeneities, so its prediction becomes inaccurate for cases of high-volume fractions. The Mori-Tanaka scheme indirectly considers inhomogeneity interactions by assuming the average matrix strain as the reference to solve for particle's average strain [9]. The present iBEM model provides more accurate predictions by directly considering

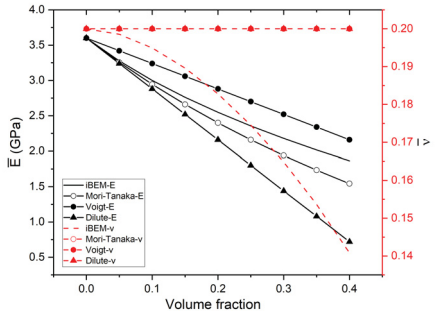

Figure 6: Effective moduli with variation of volume fraction of air voids and comparison of the Mori-Tanaka, Dilute, and Voigt models. The solid lines show the Young's modulus, while the dashed lines show Poisson's ratio.

both the interactions and boundary effect. The comparison of effective Poisson's ratios, three micromechanical schemes provides exactly same predictions of constant 0.2 for this specific problem, when the shear modulus of inhomogeneity is 0. However, it is apparent in our iBEM simulation, the Poisson's ratio is not a constant with the increase of the porosity, which shows the limitations of the three conventional micromechanical models in this special cases.

Shown in Fig.7 (a)-(d), the homogenization of concrete panels with 40% volume fraction of air voids exhibits larger maximum deflections of the bottom surface, which is opposite to our initial prediction that homogenization should provide higher effective Young's modulus and thus smaller deflections. Such phenomenons can be interpreted as:

(i) The boundary condition in panel bending is different from the uniaxial loading. The interaction between the structure and material behavior will make the size effect of air void much more complex, so that the homogenized solution cannot accurately predict the structure behavior when the air void is not too small compared to the thickness of the LWC panel;

(ii) As an extreme case, when one row of voids in the midplane of a beam, because the stress is indeed small in bending, the composite beam with air voids perform like a I-shape beam with the top and bottom layers carrying more load;

(iii) Effective properties are generally obtained through a surface average method. In the panel, due to the boundary effect, the effective Young's moduli in-plane and out-of-plane will be different from the homogenized solution, which is calculated from the cubic sample with many voids in Section 5.1. In general, the out-of-plane modulus shall be smaller than the in-plane one.

Although the homogenization method could provide a more efficient analysis as solving a homogeneous bi-material system, the approach is not good at predicting local maximum changes and may provide misleading results for the panel deflection when the particle size is not very small in comparison with the small thickness of the panel. In contrast, the present iBEM can provide the local field and the deflection. Subsequently, Fig.8 (a) shows the variation of deflection along $x_2 \in [0, 0.1]$ m versus different volume fractions. Similar to the 40% volume fraction case, homogenized solutions of 10% and 20% have larger predictions on deflection. Shown in Fig.8 (b), the maximum deflection is linearly proportional to volume fraction, in both homogenized solutions and numerical solutions with 400 equal-sized air voids. In addition, the deflection at the center of line $x_1 = 0.05$ m is minimum due to symmetric edge constraints and it follows a similar pattern as maximum deflection.

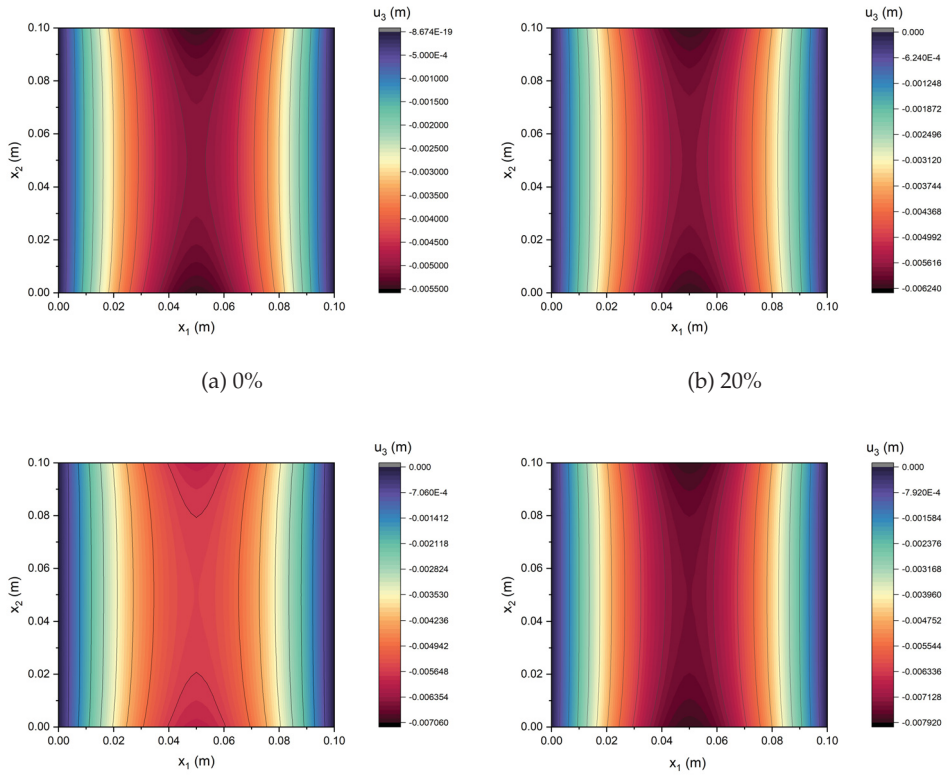

(a) 0%

(b) 20%

(c) 40%

(d) 40% - homogenized

Figure 7: Contour plots of deflection u_3 at the bottom surface of the simply supported BIPV under uniform downward pressure 1 MPa with (a) homogeneous, (b) 20%, (c) 40% and (d) 40% homogenized concrete panel with volume fraction of uniformly distributed equal-sized air voids

(c) Effects with inhomogeneity size variation

In Section (b), virtual experiments indicate volume fraction of air voids play an important role in deflections. Following the same case study of 40% volume fraction with 400 equal-sized air voids, Fig.9 shows that the size effects of inhomogeneities on effective elasticity. A cubic sample containing the same volume fraction with different sizes or numbers of air voids is tested numerically. The samples with smaller inhomogeneities or larger number of particles provide better homogenization with a larger effective Young's modulus. Indicated as Fig.9, consider a cubic concrete matrix with length 1 m containing $8, 64, 125, 512, 1,000, 3,375, 8,000$ and $15,675$ uniformly distributed equal-sized air voids of volume fraction 40%, the effective Young's modulus and Poisson's ratio varies within $[1.62, 1.88]$ and $[0.137, 0.179]$, respectively. When the number of inhomogeneities is low, i.e $8, 64$, the difference of effective properties between "number step" is relatively large. However, as the number of inhomogeneities increases, i.e $1,000, 3,375$, the difference becomes much smaller as 0.88%. Small fluctuation is observed among cases $3,375, 8,000$ and $15,625$ and if taking case $15,625$ as reference, the differences are $0.24717\%, 0.22853\%$ and $0.05023\%, 0.52049\%$ for effective Young's modulus $\overline{E}$ and Poisson's ratio $\overline{\nu}$, respectively. In terms of industrial applications, when the number of inhomogeneities is larger than $1,000$, the predictions are acceptable with tolerance less than 0.8%.

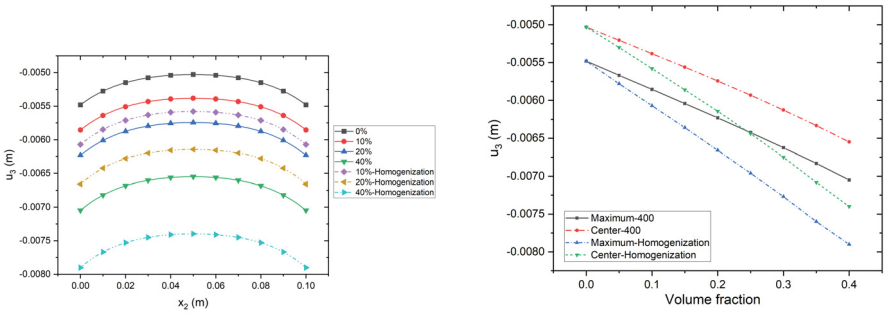

(a) (b)

Figure 8: Variation of deflection u_3 at the bottom surface along $x_2 \in [0, 0.1]$ m of the simply supported BIPV under uniform downward pressure 1 MPa with volume fraction $[0, 40]\%$ of uniformly distributed equal-sized air voids

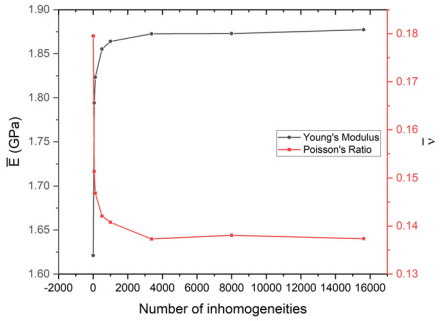

Figure 9: Effective moduli of the same volume fraction 40% uniformly distributed equal-sized air voids versus the different numbers of inhomogeneities embedded in cubic concrete matrix

In this section, the numbers are enlarged as $3,200$ and $10,800$. To minimize other effects resulting from change of microstructure, the uniform distributions are retained through shrinking even cells in Section (b) 2 and 3 times, respectively. Exhibited in Figs.7 (c)-(d) and Figs.10 (a)-(b), the contour plot of deflection shows an apparent trend that smaller voids with the same volume fraction lead to larger deflection, which agrees well with the previous conclusion on homogenized solutions with the largest deflection. The size variation with uniform distribution retains similar patterns of deflection.

To demonstrate that iBEM is capable of providing both local and global averaged solutions, Fig.11 plot contours of displacement components u_3 at the middle plane of the concrete panel with 400 and $10,800$ inhomogeneities. Notice that for case "10,800", the inhomogeneities are divided into three layers, thus only $3,600$ inhomogeneities were displayed in Fig.11(b). Unlike the previous contour plots of deflections on boundary, internal field points require both BIEs and domain integrals of the fundamental solution. Since the displacements inside an air void have no physical meaning, the circular cross sections are left blank. To describe variations in the neighborhood of cross sections, 21 points are placed on circumferences and entirely $17,001$ and

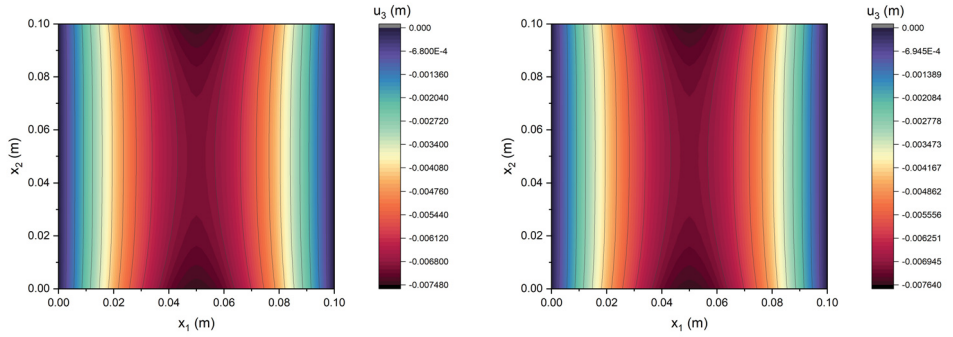

(a) $3,200$ inhomogeneities (b) $10,800$ inhomogeneities

Figure 10: Contour plots of deflection u_3 at the bottom surface of the simply supported BIPV under uniform downward pressure 1 MPa with 40% volume fraction of (a) $3,200$, (b) $10,800$ uniformly distributed air voids

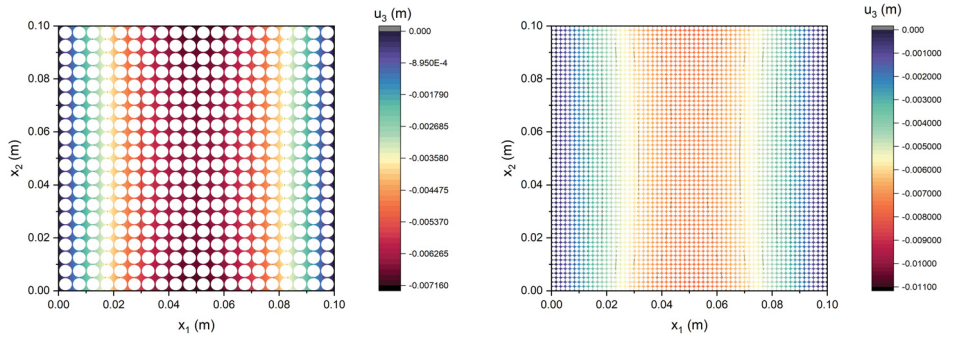

(a) 400 inhomogeneities (b) $10,800$ inhomogeneities

Figure 11: Contour plots of deflection u_3 at the central plane of the concrete panel under uniform downward pressure 1 MPa with 40% volume fraction of (a) 400, (b) $10,800$ uniformly distributed air voids

$77,001$ points are employed in Fig.11(a) and Fig.11(b), respectively. Comparing with deflection of bottom surface in Fig. 8(c), Fig.10 (a) and Fig. 10(b), the largest difference are 8×10^{-5} and 2.46×10^{-3} m for 400 and $10,800$ case, respectively, and the maximum u_3 occurs at the exactly same place, which is mainly caused by inhomogeneity interactions. As for case 400, the interactions exists merely as horizontal direction while in case $10,800$, intensive vertical interactions are also involved.

As indicated in Fig.12, the variation of deflection is plotted along $x_1 = 0.05$ m when $x_2 \in [0, 0.1]$ m. When the size of inhomogeneities shrinks, the deflection increases and gradually moves close to the homogenized solution. In addition, the differences in maximum deflection between the number of steps suggests that a large number of inhomogeneities is prequesite for homogenized solution. Therefore, given a prescribed microstructure with limited number of inhomogeneities, using the homogenized solution may lead to overestimates.

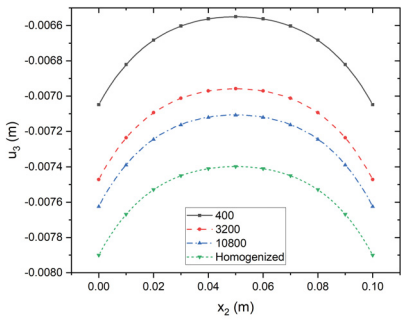

Figure 12: Variation of deflection u_3 at the bottom surface along $x_2 \in [0, 0.1]$ m of the simply supported BIPV under uniform downward pressure 1 MPa with 40% volume fraction of uniformly distributed $400, 3, 200, 10, 800$ equal-sized air voids

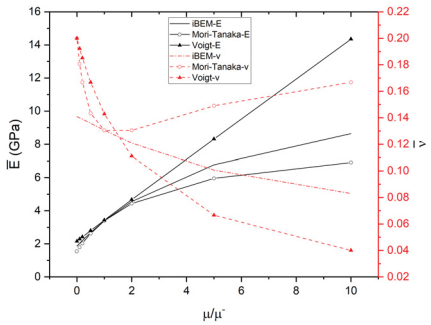

Figure 13: Effective moduli with variation of shear modulus μ/μ^- ratio between inhomogeneity and matrix containing 40% volume fraction of inhomogeneities and comparison with the Mori-Tanaka and Voigt models

(d) Effects with ratio of shear moduli

This subsection aims to investigate how the ratio of shear moduli influences the bi-layered composites. Following the case study in the last subsection, consider 400 equal-sized inhomogeneities are uniformly distributed with radius 2.28 mm, and the volume fraction remains the same as 40%. In the following, 7 ratios of shear moduli, $0.1, 0.2, 0.5, 1, 2, 5$ and 10, are considered and the Poisson's ratio for inhomogeneities are set as 0. As shown in Fig.13, the homogenized properties are calculated by iBEM and compared with Mori-Tanaka and Voigt schemes. The curve "iBEM-E" and "iBEM-ν" stays between the two micromechanical models when $\mu/\mu^- > 2$. Fig.14 (a) shows the variation of deflection along $x_1 = 0.05$ m with $x_2 \in [0, 0.1]$ m, when μ/μ^- increases, the maximum deflection reduces significantly the difference between case 0.1 and case 10 reaches 2.35 mm. Unlike the effects of volume fraction, the maximum/center deflection versus ratio of shear moduli exhibits a decreasing slope. Compared with homogenized solutions, two branches of phenomenon are observed when $\mu/\mu^- < 1$, homogenized solutions have larger deflections and vice versa.

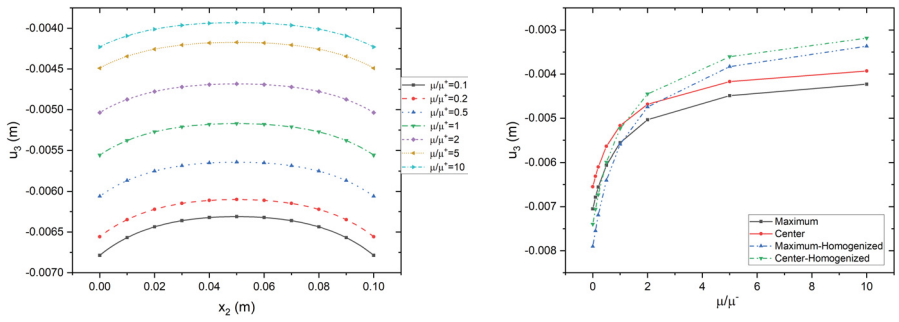

(a) (b)

Figure 14: Variation of deflection u_3 at the bottom surface along $x_2 \in [0, 0.1]$ m of the simply supported BIPV under uniform downward pressure 1 MPa with 40% volume fraction of uniformly distributed equal-sized inhomogeneities whose shear modulus ratio $\mu/\mu^- \in [0, 10]$

(e) Effects with inhomogeneity distribution

In the previous three sections, equal-sized inhomogeneities are uniformly distributed over the concrete panel. However, due to the limitations of manufacture, it is not likely that all inhomogeneities are with the same dimension and are uniformly distributed. Shown in Fig.15, $4,638$ inhomogeneities with radius ranging $[0.668, 2]$ mm are randomly distributed. Without the loss of any generality, the uniform possibility density function is selected. Fig.16 compares the center deflection and the maximum deflection at different volume fractions, where the "center" and "maximum" mean the deflection at the center point and the maximum deflection of the bottom surface, respectively; and "homogenized" means the size of inhomogeneities are equal to each other. It can be found that all the deflections (absolute values) increase with the volume fraction increasing. Besides, for both "center" and "maximum" deflections, the equal-sized inhomogeneities distribution structures come out with higher deflection compared with those with different sizes. Especially, when the volume fraction is in the specific range, say $5\% - 35\%$, the size effect on the maximum deflection is approximately 8% lower than other range of volume fraction, which means that we should pay more attention to the air void size when manufacturing a BIPV panel within the accordingly volume fraction range.

6. Conclusions

The inclusion-based boundary element method (iBEM) has been used to investigate mechanical properties of bi-layered systems with single-domain boundary integral method. Through the combination of BEM and EIM, the conventional boundary value problem of inhomogeneities coupling with various boundary conditions can be solved without internal subdomain mesh or the bi-material interface. It provides a powerful tool for virtual experiments of actual material samples, which is verified by the FEM for the simple cases with one or few particles and is then extended to over $10,000$ particles for the numerical mechanical experiments. With the Taylor series expansion of continuous eigenstrain field, every single inhomogeneity can be replaced with a constant number of unknown eigenstrains, which provides tailorable accuracy with the order of the Taylor expansion. The parametric studies are conducted on microstructural effects, inhomogeneity size variation, volume fraction, ratio of shear moduli and distribution with the following highlights:

1. For material homogenization, a cubic material sample containing uniformly distributed air

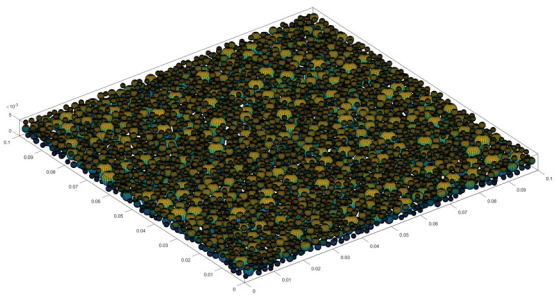

Figure 15: Schematic plot of concrete panel containing $4,638$ randomly distributed inhomogeneities with radius ranging $[0.5a, 1.5a](a = 1.336)$ mm

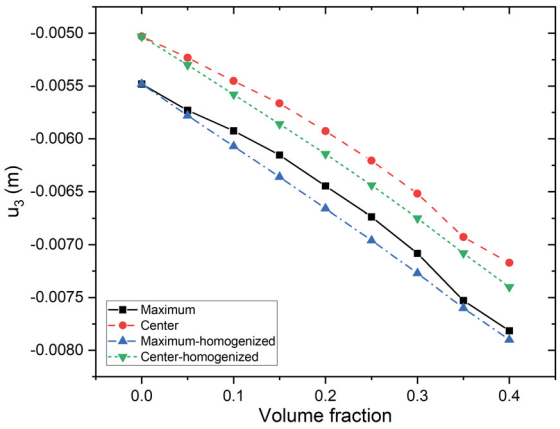

Figure 16: Comparison of deflection u_3 versus volume fraction ranging $[0, 40]$ % between solutions with homogenized properties and randomly distributed inhomogeneities with radius ranging $[0.5, 1.6]a$ ($a = 1.336$ mm)

voids at 40% volume fraction exhibits increasing Young's modulus with the number of air voids, when the number reaches 1000, the results become convergent with 0.8%;

2. Although a cubic sample with a small number of voids exhibits a smaller Young's modulus under uniaxial loading tests, it shows higher flexural resistance in the bi-layered panel bending test as the void periodically distributed in the center of cubic unit cells;

3. The test coupons with a concrete substrate containing 400 and $10,800$ air voids at 40% volume fraction exhibit 0.00706 and 0.00764 m of the maximum deflection;

4. Given a volume fraction and the number of voids, the narrow variation of the void size exhibits higher maximum deflection of the panel.

Given the microstructure of the composite material the cross-scale modeling of the structural response of bi-layered composites is demonstrated by the iBEM, which provides a powerful tool for virtual experiments of new material and structure design and analysis.

References

1. Eshelby JD. 1957 The determination of the elastic field of an ellipsoidal inclusion, and related problems. *Proceedings of the Royal Society of London. Series A. Mathematical and Physical Sciences* **241**, 376–396.
2. Eshelby JD. 1959 The elastic field outside an ellipsoidal inclusion. *Proceedings of the Royal Society of London. Series A. Mathematical and Physical Sciences* **252**, 561–569.
3. Mura T. 1987 *Micromechanics of defects in solids*. Dordrecht: Springer Netherlands.
4. Dyson FW. 1891 The potentials of ellipsoids of variable densities. *The Quarterly Journal of Pure and Applied Mathematics*.
5. Jarali CS, Madhusudan M, Vidyashankar S, Raja S. 2018 A new micromechanics approach to the application of Eshelby's equivalent inclusion method in three phase composites with shape memory polymer matrix. *Composites Part B: Engineering* **152**, 17–30.
6. Hill R. 1965 A self-consistent mechanics of composite materials. *Journal of the Mechanics and Physics of Solids* **13**, 213–222.
7. Affdl JCH, Kardos JL. 1976 The Halpin-Tsai equations: A review. *Polymer Engineering and Science* **16**, 344–352.
8. Mori T, Tanaka K. 1973 Average stress in matrix and average elastic energy of materials with misfitting inclusions. *Acta Metallurgica* **21**, 571–574.
9. Yin H, Zhao Y. 2016 *Introduction to the Micromechanics of Composite Materials*. Boca Raton: CRC Press.
10. sheng Yang Q, qiao He X, Liu X, fang Leng F, Mai YW. 2012 The effective properties and local aggregation effect of CNT/SMP composites. *Composites Part B: Engineering* **43**, 33–38.
11. Imani SM, Goudarzi A, Rabiee SM, Dardel M. 2018 The modified Mori-Tanaka scheme for the prediction of the effective elastic properties of highly porous ceramics. *Ceramics International* **44**, 16489–16497.
12. Song Z, Peng X, Tang S, Fu T. 2020 A homogenization scheme for elastoplastic composites using concept of Mori-Tanaka method and average deformation power rate density. *International Journal of Plasticity* **128**, 102652.
13. Liu YJ, Song G, Yin HM. 2015 Boundary effect on the elastic field of a semi-infinite solid containing inhomogeneities. *Proceedings of the Royal Society A: Mathematical, Physical and Engineering Sciences* **471**, 20150174.
14. Wu C, Zhang L, Yin H. 2022 Stress concentration of a micro-void embedded in a bi-layered material considering the boundary effects (In press). *Journal of Engineering Mechanics*.
15. Wu C, Yin H. 2021 The inclusion-based boundary element method (iBEM) for virtual experiments of elastic composites. *Engineering Analysis with Boundary Elements* **124**, 245–258.
16. Hill R. 1963 Elastic properties of reinforced solids: Some theoretical principles. *Journal of the Mechanics and Physics of Solids* **11**, 357–372.
17. Yang S, Dirrenberger J, Monteiro E, Ranc N. 2019 Representative volume element size determination for viscoplastic properties in polycrystalline materials. *International Journal of Solids and Structures* **158**, 210–219.
18. Kanit T, Forest S, Galliet I, Mounoury V, Jeulin D. 2003 Determination of the size of the representative volume element for random composites: statistical and numerical approach. *International Journal of Solids and Structures* **40**, 3647–3679.
19. Terada K, Hori M, Kyoya T, Kikuchi N. 2000 Simulation of the multi-scale convergence in computational homogenization approaches. *International Journal of Solids and Structures* **37**, 2285–2311.
20. Gusev AA. 1997 Representative volume element size for elastic composites: A numerical study. *Journal of the Mechanics and Physics of Solids* **45**, 1449–1459.
21. Dirrenberger J, Forest S, Jeulin D. 2014 Towards gigantic RVE sizes for 3D stochastic fibrous networks. *International Journal of Solids and Structures* **51**, 359–376.
22. Sakata S, Ashida F, Kojima T. 2008 Stochastic homogenization analysis on elastic properties of fiber reinforced composites using the equivalent inclusion method and perturbation method. *International Journal of Solids and Structures* **45**, 6553–6565.
23. Sakata S, Ashida F, Kojima T. 2010 Stochastic homogenization analysis for thermal expansion coefficients of fiber reinforced composites using the equivalent inclusion method with perturbation-based approach. *Computers & Structures* **88**, 458–466.
24. Chen Q, Wang G, Chen X, Geng J. 2017 Finite-volume homogenization of elastic/viscoelastic periodic materials. *Composite Structures* **182**, 457–470.

25. Sfantos G, Aliabadi M. 2007 Multi-scale boundary element modelling of material degradation and fracture. *Computer Methods in Applied Mechanics and Engineering* **196**, 1310–1329.
26. Zhou K, Keer L, Wang QJ. 2011 Analysis of hard coatings on a substrate containing inhomogeneities. *Journal of Mechanics of Materials and Structures* **6**, 627–639.
27. Dong Q, Chen Z, Zhou K, He D. 2021 Fretting contact of layered materials with vertical cracks near surfaces. *International Journal of Mechanical Sciences* **198**, 106361.
28. Treifi M, Oyadiji SO. 2013a Bi-material V-notch stress intensity factors by the fractal-like finite element method. *Engineering Fracture Mechanics* **105**, 221–237.
29. Treifi M, Oyadiji SO. 2013b Evaluation of mode III stress intensity factors for bi-material notched bodies using the fractal-like finite element method. *Computers & Structures* **129**, 99–110.
30. Bouhala L, Shao Q, Koutsawa Y, Younes A, Núñez P, Makradi A, Belouettar S. 2013 An XFEM crack-tip enrichment for a crack terminating at a bi-material interface. *Engineering Fracture Mechanics* **102**, 51–64.
31. Pathak H, Singh A, Singh IV. 2011 Numerical simulation of bi-material interfacial cracks using EFGM and XFEM. *International Journal of Mechanics and Materials in Design* **8**, 9–36.
32. Wu Z, Lin Q, Chen Y. 2020 Application of fast multipole boundary element method for two-dimensional nonlinear interface debonding of particulate composites. *Engineering Analysis with Boundary Elements* **113**, 72–81.
33. Legrain G. 2013 A NURBS enhanced extended finite element approach for unfitted CAD analysis. *Computational Mechanics* **52**, 913–929.
34. Beer G, Dünser C, Ruocco E, Mallardo V. 2020 Efficient simulation of inclusions and reinforcement bars with the isogeometric Boundary Element method. *Computer Methods in Applied Mechanics and Engineering* **372**, 113409.
35. Liu YJ, Mukherjee S, Nishimura N, Schanz M, Ye W, Sutradhar A, Pan E, Dumont NA, Frangi A, Saez A. 2011 Recent Advances and Emerging Applications of the Boundary Element Method. *Applied Mechanics Reviews* **64**.
36. Yin H, Song G, Zhang L, Wu C. 2022 Chapter 5 - The iBEM formulation and implementation: Ellipsoidal inhomogeneities in a bounded domain. In *The Inclusion-Based Boundary Element Method (iBEM)* pp. 147–168. Cambridge: Academic Press.
37. Yue ZQ. 1995a On generalized Kelvin solutions in a multilayered elastic medium. *Journal of Elasticity* **40**, 1–43.
38. Yue Z. 1995b Elastic fields in two joined transversely isotropic solids due to concentrated forces. *International Journal of Engineering Science* **33**, 351–369.
39. qi Quentin Yue Z. 2015 Yue's solution of classical elasticity in n-layered solids: Part 1, mathematical formulation. *Frontiers of Structural and Civil Engineering* **9**, 215–249.
40. Xiao S, Yue ZQ, Xiao H. 2019 Boundary element analysis of transversely isotropic bi-material halfspaces with inclined planes of isotropy and interfaces. *International Journal for Numerical and Analytical Methods in Geomechanics* **43**, 2599–2627.
41. Xiao S, Yue ZQ. 2020 Boundary element formulation of axisymmetric problems in vertically non-homogeneous solids subject to normal traction. *Engineering Analysis with Boundary Elements* **114**, 178–195.
42. Walpole L. 1996 An elastic singularity in joined half-spaces. *International Journal of Engineering Science* **34**, 629–638.
43. Wu C, Zhang L, Cui J, Yin H. 2023 Three-dimensional elastic analysis of a bi-material system with a single domain boundary element method. *Engineering Analysis with Boundary Elements* **146**.
44. Barber J. 1992 *Elasticity*. Dordrecht: Springer Dordrecht.
45. Yin H, Zadshir M, Pao F. 2021 *Building Integrated Photovoltaic Thermal Systems*. Cambridge: Academic Press.
46. Li Y, Xie L, Zhang T, Wu Y, Sun Y, Ni Z, Zhang J, He B, Zhao P. 2020 Mechanical analysis of photovoltaic panels with various boundary condition. *Renewable Energy* **145**, 242–260.

Ethics. The authors declare that there is no disobeying of ethics in the paper.

Data Accessibility. All data, models, or code that support the findings of this study are available from the corresponding author upon reasonable request.

Authors' Contributions. **Chunlin Wu**: Methodology, Data Curation, Software, Validation, Writing-Original Draft; **Liangliang Zhang**: Resources, Methodology, Writing-Review & Editing, Supervision; **Huiming Yin**: Conceptualization, Methodology, Writing-Review & Editing, Supervision.

Competing Interests. The authors declare that they have no known competing financial interests or personal relationships that could have appeared to influence the work presents in this paper.

Funding. National Science Foundation IIP #1738802, IIP #1941244, CMMI#1762891, U.S. Department of Agriculture NIFA #2021-67021-34201, and National Natural Science Foundation of China (Grant No. 12102458)

Acknowledgements. This work is sponsored by the National Science Foundation IIP #1738802, IIP #1941244, CMMI#1762891, U.S. Department of Agriculture NIFA #2021-67021-34201, and National Natural Science Foundation of China (Grant No. 12102458), whose support is gratefully acknowledged. We also thank Linda Getachew Teka for her proofread of the paper, whose suggestion and comments are gratefully acknowledged.

Disclaimer. Not Applicable.